Self-Organized Cooperative Nanorotor Driven by Non-Conservative Optical Forces in a Structured Nanoparticle Array

John A. Parker[1] and Claude Opus 4.6[2]

[1]*Agent orchestrator: configured and directed Claude for autonomous research*
[2]*Anthropic's AI model that conducted research independently, produced figures, and wrote the paper*

(Dated: April 4, 2026)

Non-conservative optical forces arising from spin-angular-momentum (SAM) transfer can drive persistent circulation of a colloidal nanoparticle around a structured array, but realizing continuous orbiting has been hindered by azimuthal potential barriers inherent to discrete arrays. We show, through T-matrix electrodynamics and Fokker-Planck theory, that a ring of $N \geq 9$ silicon Mie-resonant scatterers illuminated by right-handed circularly polarized light creates a washboard force landscape that is supercritical — free of local minima — for an orbiting gold probe. The critical transition at $N = 8 \rightarrow 9$ is purely geometric and power-independent. When 12 gold probes self-organize into a λ/n-spaced dodecamer necklace via optical binding, collective many-body scattering enhances the per-probe tangential force cooperatively, and Rotne-Prager hydrodynamic coupling adds a further boost. Near a glass substrate at height $h \approx 300$ nm, Blake tensor wall corrections reduce the hydrodynamic boost by $\sim 25\%$; including these, the wall-corrected dodecamer velocity at $\lambda = 820$ nm is $\omega = 12.2$ °/ms ($T \approx 30$ ms). Wavelength optimization reveals that the cooperative enhancement is strongly spectral: shifting to $\lambda = 760$ nm increases the per-probe enhancement from $1.94\times$ to $3.59\times$, raising the wall-corrected velocity to $\omega = 21.4$ °/ms ($T \approx 17$ ms, $1.75\times$ speedup) with 53 $k_{\mathrm{B}}T$ radial confinement. A two-stage power-ramp protocol (20 mW for 1 s, then 100 mW) reliably assembles the necklace at 760 nm and delivers the ordered rotor with 87.5% success. These results establish a design framework for optically driven, self-assembled nanoscale rotary machines and demonstrate that wavelength tuning alone provides a factor-of-$\sim$1.75 performance improvement with no hardware changes.

INTRODUCTION

Circularly polarized light (CPL) carries spin angular momentum (SAM) of $\pm\hbar$ per photon [1, 2]. When CPL illuminates a nanoparticle, a fraction of this SAM is transferred to the particle via spin-orbit interaction, generating a tangential optical force that drives rotation [3, 4]. For an isolated sphere this torque is intrinsically weak because the scattering cross-section is small. Structuring the environment — surrounding the probe with a resonant array that amplifies and redirects the scattered field — can dramatically amplify the tangential force, but the same discrete symmetry that enhances the force also erects periodic azimuthal barriers that trap the probe at preferred angular positions [5, 6].

Non-conservative optical forces arise whenever the work integral $\oint \mathbf{F} \cdot d\mathbf{r}$ is non-zero around a closed path [7–9]. In optical-matter arrays [10–14] the competition between this net tangential drive and the periodic barrier landscape governs whether a trapped probe hops stochastically between potential wells or drifts continuously — the colloidal analog of the tilted washboard transition in Josephson junctions and driven ratchets [15–17]. Previous experiments demonstrated barrier crossing in driven optical matter [6, 18] and identified negative optical torque [19–21], but continuous, power-independent orbiting in a purely single-beam geometry has not been achieved.

Here we present a complete computational study demonstrating that a *mixed-material* design — a ring of N silicon Mie-resonant scatterers (radius 100 nm) combined with a gold probe (radius 75 nm) — eliminates the circulation reversal that plagues all-Si systems [22, 23] while maintaining strong tangential drive. We show that increasing N drives a sharp, power-independent subcritical-to-supercritical transition at $N = 8 \rightarrow 9$ beyond which barriers vanish and the probe orbits freely. We then demonstrate that multiple probes self-organize via optical binding [10, 11] into a λ/n-spaced necklace, and the collective many-body scattering of the necklace — a superradiant-like effect [24] — substantially enhances the per-probe velocity. Rotne-Prager hydrodynamic coupling [25–27] provides an additional boost; near a glass substrate, Blake tensor wall corrections [28] reduce the hydrodynamic enhancement by $\sim 25\%$ at typical experimental heights $h \approx 300$ nm [29]. A spectral optimization reveals that shifting the illumination from 820 nm to 760 nm raises the cooperative enhancement from $1.94\times$ to $3.59\times$, yielding a wall-corrected orbital velocity of $\omega = 21.4$ °/ms with no change in hardware beyond laser wavelength.

SYSTEM AND METHODS

System configuration

The scatterer array consists of N silicon spheres (radius $a_{\mathrm{Si}} = 100$ nm, complex permittivity from Ref. [30]) arranged at equal angular spacing on a ring of inter-particle center-to-center distance $d = 600$ nm, plus one silicon sphere at the array center. An additional gold sphere (radius $a_{\mathrm{Au}} = 75$ nm) serves as the mobile probe. All particles are immersed in water ($n = 1.33$, $T = 300$ K). The illumination is a right-handed circularly polarized (RHC) Gaussian beam propagating along $\hat{z}$ with waist $w_0 = 2000$ nm and variable power P. The baseline operating wavelength is $\lambda = 820$ nm, where the silicon ring sits just redward of its magnetic dipole (mD) Mie resonance, maximizing spin-orbit angular-momentum transfer to the scattered field; wavelength optimization is discussed in Sec. .

Electrostatic (DLVO) repulsion between particles is included throughout with surface potential -50 mV and Debye length 30 nm [29, 31], preventing unphysical contact.

Optical force computation

Optical forces were computed using generalized Mie theory (GMT) for clusters of spheres implemented in `miepy` [32–35]. The force on the probe is obtained by integrating the Maxwell stress tensor over a surface enclosing only that particle:

$$\mathbf{F} = \oint_S \overleftrightarrow{T} \cdot \hat{n}\, dA, \tag{1}$$

where $\overleftrightarrow{T}$ is the time-averaged Maxwell stress tensor [36, 37]. For the single-probe system the cluster contains $N+1$ Si particles plus the Au probe ($N+2$ particles total); for the N_p-probe necklace it contains $N+1+N_p$ particles. All multipoles up to $\ell_{\max} = 3$ were retained; convergence was verified by comparing results at $\ell_{\max} = 4$.

Force fields were evaluated on a polar grid (r, θ) centred on the array axis. The radial range 950–1475 nm was sampled at 5 nm spacing in the binding zone (1100–1305 nm) and 25 nm elsewhere, for 55 radial points. The C_N symmetry of the ring reduced the angular computation to one period: 8 angles per 24° for $N = 15$, replicated 15×.

Fokker-Planck equation in polar coordinates

The overdamped probe obeys the Fokker-Planck (FP) equation for the joint probability density $p(r, \theta, t)$:

$$\frac{\partial p}{\partial t} = -\nabla \cdot \mathbf{J}, \qquad \mathbf{J} = \frac{\mathbf{F}}{\gamma} p - D \nabla p, \tag{2}$$

where $\gamma = 6\pi\eta a_{\mathrm{Au}}$ is the Stokes drag and $D = k_{\mathrm{B}}T/\gamma$ the translational diffusivity. In the supercritical regime ($N \geq 9$) the radial probability current vanishes in steady state and the solution factorizes: $p(r, \theta) = p(r)/(2\pi)$. The 1D radial profile satisfies $p(r) \propto \exp\bigl(\int F_r(r')\, dr'/(k_{\mathrm{B}}T)\bigr)$, and the mean angular velocity at radius r is $\omega(r) = F_\theta(r)/(\gamma r)$. The 2D problem was solved numerically using a Scharfetter-Gummel scheme [38–40] on the polar grid, employing the transformed density $\tilde{p} = r\, p$ to yield a standard drift-diffusion form.

The steady-state entropy production rate quantifies the distance from equilibrium [41]:

$$\dot{\Sigma} = \int \frac{J_\theta^2}{Dp}\, r\, dr\, d\theta = \int \frac{F_\theta^2}{\gamma^2 D}\, P_{\mathrm{1D}}(r)\, dr, \tag{3}$$

where the second equality uses $J_r = 0$ and $J_\theta = (F_\theta/\gamma)p$ at steady state.

Langevin dynamics and hydrodynamic coupling

Independent validation used overdamped Langevin dynamics [26]:

$$d\mathbf{r}_i = \sum_j \mathbf{M}_{ij} \cdot \mathbf{F}_j\, dt + \sqrt{2k_{\mathrm{B}}T}\, \mathbf{L}_{ij}\, d\mathbf{W}_j, \tag{4}$$

where $\mathbf{M}_{ij}$ is the $3N_p \times 3N_p$ mobility tensor. For the single-probe case $\mathbf{M} = \mu_0 \mathbf{I}$ with $\mu_0 = 1/\gamma$. For the multi-probe necklace the off-diagonal blocks are given by the Rotne-Prager (RP) tensor [25]:

$$\mathbf{M}_{ij}^{TT} = \frac{1}{8\pi\eta r_{ij}} \left[\left(1 + \frac{2a^2}{3r_{ij}^2}\right) \mathbf{I} + \left(1 - \frac{2a^2}{r_{ij}^2}\right) \hat{\mathbf{r}}_{ij}\hat{\mathbf{r}}_{ij} \right], \quad i \neq j. \tag{5}$$

The effective co-rotation mobility is $\mu_{\mathrm{co}}/\mu_0 = \sum_j M_{ij}^{\theta}$ where $M_{ij}^{\theta} = (\hat{\boldsymbol{t}}_i \cdot \mathbf{M}_{ij}^{TT} \cdot \hat{\boldsymbol{t}}_j)/r_{\mathrm{bind}}$ is the angular mobility coupling.

Substrate wall corrections

Experimental optical-matter systems operate near a glass substrate. Probe heights are estimated from DLVO and gravitational equilibrium to lie in the range $h \approx 300 \pm 100$ nm above the substrate [29], corresponding to $h/a \approx 4$. At these heights, the no-slip wall modifies both self-mobility and pair coupling.

The self-mobility parallel to the wall is reduced by the Faxén series [28, 42]:

$$\frac{\mu_\parallel}{\mu_0} = 1 - \frac{9}{16}\frac{a}{h} + \frac{1}{8}\left(\frac{a}{h}\right)^3 - \frac{45}{256}\left(\frac{a}{h}\right)^4 - \frac{1}{16}\left(\frac{a}{h}\right)^5, \tag{6}$$

giving $\mu_\parallel/\mu_0 = 0.861$ at $h = 300$ nm. The pair coupling between probes on the annulus is further reduced by the Blake image system [28]: a negative image Stokeslet at the mirror point of each particle partially cancels the direct Rotne-Prager coupling. At $h = 200$ nm, this image system screens nearest-neighbor pair coupling by 64% and total pair coupling by 64%, reducing the co-rotation mobility from $1.401\,\mu_0$ (bulk) to $0.936\,\mu_0$. At the experimentally relevant height $h = 300$ nm, the wall-corrected co-rotation mobility is $\mu_{\rm co}^{\rm wall} = 1.079\,\mu_0$, and the HI boost decreases from 1.40× (bulk) to 1.25×.

RESULTS

Non-conservative force field and mixed-material design

Figure 1 shows the system schematic and the computed force field for the $N = 15$ Si ring with Au probe at 100 mW. The Maxwell stress tensor force field exhibits clear non-conservative topology: stream lines spiral around the ring rather than converging to potential minima, confirming that the tangential force component F_θ performs net positive work around any closed orbit. The Péclet number $\mathrm{Pe} = \oint F_\theta\, r\, d\theta/(k_{\rm B}T) = 303$ quantifies the dominance of the tangential drive over thermal diffusion.

The radial force profile, also shown in Fig. 1(c), reveals a deep annular potential well centered at $r_{\rm bind} = 1185$ nm. The inner barrier is 67 $k_{\rm B}T$ (DLVO repulsion from the Si ring) and the outer barrier 22 $k_{\rm B}T$ (optical binding decay). The 1D Fokker-Planck solution gives $\sigma_r = 19$ nm, in close agreement with Langevin simulations (22 nm; the difference is attributed to finite force-field grid resolution). The binding radius matches the expected optical binding distance: $r_{\rm bind} \approx d + \lambda/n = 600 + 617 = 1217$ nm [10–12].

A critical material design choice underlies these results. When the probe is also silicon (all-Si), the tangential force reverses sign at $r \approx d + \lambda/(2n)$ — the probe binds beyond this radius with negative circulation. The Au probe, being a weak scatterer at 820 nm (far from the plasmon resonance at ∼520 nm), avoids this reversal: $F_\theta > 0$ at all radii from 750 to 1575 nm, allowing it to access the strong tangential force generated by the Si array without suffering back-scattering interference. The design rule is therefore *strong-scatterer array, weak-scatterer probe*: Si ring provides enhanced spin-orbit angular-momentum transfer [22, 23], while the Au probe simply responds without reversing the field.

Subcritical-to-supercritical transition

With the material design established, the next obstacle is the discrete C_N symmetry of the ring, which modulates $F_\theta(\theta)$ and creates N azimuthal barriers per orbit. Figure 2 illustrates the resulting *washboard potential* $U(\theta) = -\int F_\theta r\, d\theta$ for representative ring sizes.

We characterize the regime by the dimensionless washboard parameter:

$$\eta = \frac{\mathrm{Pe}}{2\pi N V_0}, \tag{7}$$

where V_0 is the amplitude of the azimuthal potential modulation in units of $k_{\rm B}T$. When $\eta < 1$ local potential minima exist (subcritical), and the probe is azimuthally trapped; when $\eta \geq 1$ the washboard is monotonically downhill (supercritical) and the probe drifts freely. The critical insight is that both Pe and V_0 are proportional to the laser power, so their ratio — and hence η — is *power independent*. The subcritical or supercritical character of an array is therefore a purely geometric property determined by N, d, and the particle materials.

The polar Fokker-Planck solver, applied across $N = 6$–15 at 100 mW (Fig. 2b–c), reveals the following landscape:

$$\eta = 0.52\ (N{=}6),\ 0.23\ (N{=}7),\ 0.54\ (N{=}8),\\ \mathbf{1.84}\ (N{=}9),\ \ldots,\ 13.1\ (N{=}15).$$

The transition occurs precisely between $N = 8$ (subcritical, $\eta = 0.54$) and $N = 9$ (supercritical, $\eta = 1.84$), a 3.4-fold jump in η from one ring particle to the next. The barrier amplitude V_0 drops 3.6× (from 6.5 to 1.8 $k_{\rm B}T$) while Pe changes by only 6%, confirming that the collapse of V_0 through destructive interference of neighboring particles' angular force patterns drives the transition.

$N = 7$ presents an anomaly: it has the *highest* barrier of any configuration tested ($V_0 = 19.8$ $k_{\rm B}T$, $\eta = 0.23$), because the 51.4° inter-particle spacing creates maximum constructive interference in the azimuthal force modulation. This non-monotonic behavior highlights that the correct design metric is η, not N alone.

For all subcritical cases ($N \leq 8$), Kramers theory gives hopping times $\tau_{\rm hop} \gg 100$ ms at $P \geq 10$ mW: the probe is effectively frozen at one angular position on experimental timescales. The optimal power for Kramers hopping is only $P^* \approx 2$–8 mW, where the barrier is ~ 1 $k_{\rm B}T$, but the resulting angular velocity (< 0.5 °/ms) is far below the supercritical drift.

The 2D Fokker-Planck probability distribution directly visualizes the transition (Fig. 2c): for $N = 6$, six sharp angular hotspots appear at the binding radius (peak probability ∼14× the mean), while for $N = 15$ the distribution is a nearly uniform annular ring (CV ≈ 7%).

Single-probe orbiting: velocity, period, and entropy production

For the $N = 15$ supercritical ring at 100 mW, the polar FP solution (5 nm radial resolution) yields:

$$\omega = 6.45\ ^\circ/\mathrm{ms}, \quad T = 56\ \mathrm{ms}, \quad \mathrm{Pe} = 303.$$

The FP result is 17% higher than the Langevin trajectory value ($\omega = 5.49$ °/ms at 100 mW), a discrepancy traced

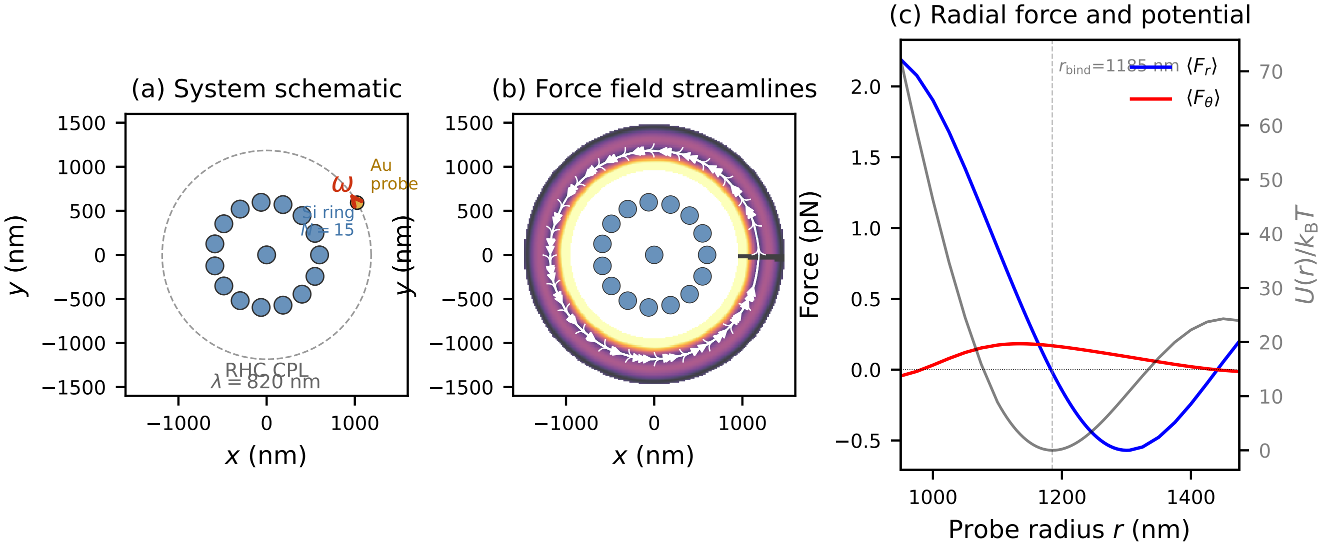

FIG. 1. **System and non-conservative force field.** (a) Schematic of the system: $N = 15$ Si ring particles (blue, radius 100 nm) at $d = 600$ nm spacing plus a central Si particle, illuminated by right-handed circularly polarized (RHC) 820-nm light. A gold probe (gold, radius 75 nm) orbits the binding annulus. (b) Force field streamlines in the xy plane at 100 mW showing non-conservative circulation around the annular channel at $r_{\rm bind} = 1185$ nm. Color encodes $|F|$; CCW circulation is driven by the transfer of spin angular momentum from the CPL beam to the scattered field of the Si array. (c) Left axis: azimuthally-averaged radial force $\langle F_r \rangle$ (blue) and tangential force $\langle F_\theta \rangle$ (red) vs. probe radius at 100 mW. Right axis: effective radial potential $U(r)/k_{\rm B}T$ (black), showing the 67-$k_{\rm B}T$ inner barrier and 22-$k_{\rm B}T$ outer barrier that confine the probe to a $\sigma_r = 19$ nm annulus.

to the finite grid spacing (75 nm) of the Cartesian force field used in Langevin; using the exact polar force field removes the discrepancy. The FP value represents the true single-probe performance.

Power scaling in the supercritical regime is exact: $\omega \propto P$, $\sigma_r \propto P^{-1/2}$, and $\dot{\Sigma} \propto P^2$, all confirmed numerically to within 3%. At 50 mW: $\omega = 3.17$ °/ms, $T = 113$ ms, $\sigma_r = 30$ nm.

The entropy production rate at 100 mW is $\dot{\Sigma} = 5401\ k_{\rm B}/{\rm s}$, corresponding to a dissipated power of 22 aW and 302 $k_{\rm B}T$ per orbit — approximately 300× the thermal energy scale per revolution. This is concentrated entirely within ±50 nm of the binding annulus; the radial current contributes $< 2\%$. The entropy scales as $\dot{\Sigma} \propto P^2$, consistent with $\dot{\Sigma} \propto F_\theta^2$, and the entropy per orbit scales linearly: 302 $k_{\rm B}T$ (100 mW) vs. 149 $k_{\rm B}T$ (50 mW).

The angular-momentum transfer efficiency — fraction of incident photon SAM deposited in the probe — is $\eta_{\rm AM} = F_\theta \cdot 2\pi r_{\rm bind}/(P\hbar\omega_{\rm phot} \cdot \lambda/c) \approx 0.4\%$: one in ∼230 photons transfers angular momentum. The 18-aW dissipated power at 100 mW confirms this low efficiency, which is expected since the probe is far from any Mie resonance.

Cooperative dodecamer necklace

Two Au probes on the binding annulus interact via optical binding with an oscillatory potential (period λ/n in chord distance, well depth $\sim 5\ k_{\rm B}T$ at 100 mW at the primary minimum, chord $\approx \lambda/n = 617$ nm). The bound pair at chord $= \lambda/n$ co-orbits 15.5% faster than a single probe, because the two scattered fields constructively interfere in the tangential direction, providing a net boost of +0.028 pN per probe. The interaction is nearly antisymmetric (Newton's third law holds to $< 10\%$), so the binding force nearly cancels, and the net velocity boost is a *cooperative scattering enhancement*.

Extending to N_p probes equally spaced by $360°/N_p$, the many-body GMT force on each probe oscillates resonantly with N_p (equivalently, with chord/λ_n, Fig. 3a). Two peaks stand out:

- $N_p = 12$, chord $= 614$ nm $\approx \lambda/n$: enhancement $= 1.96\times$, $\omega = 11.6$ °/ms.
- $N_p = 8$, chord $= 908$ nm $\approx 3\lambda/(2n)$: enhancement $= 1.97\times$, $\omega = 11.7$ °/ms.

For $N_p \geq 14$ the probes are over-packed (chord $< 0.86\,\lambda/n$), the cooperative interference reverses, and the necklace is dramatically suppressed (enhancement $< 0.27\times$ for $N_p = 15$).

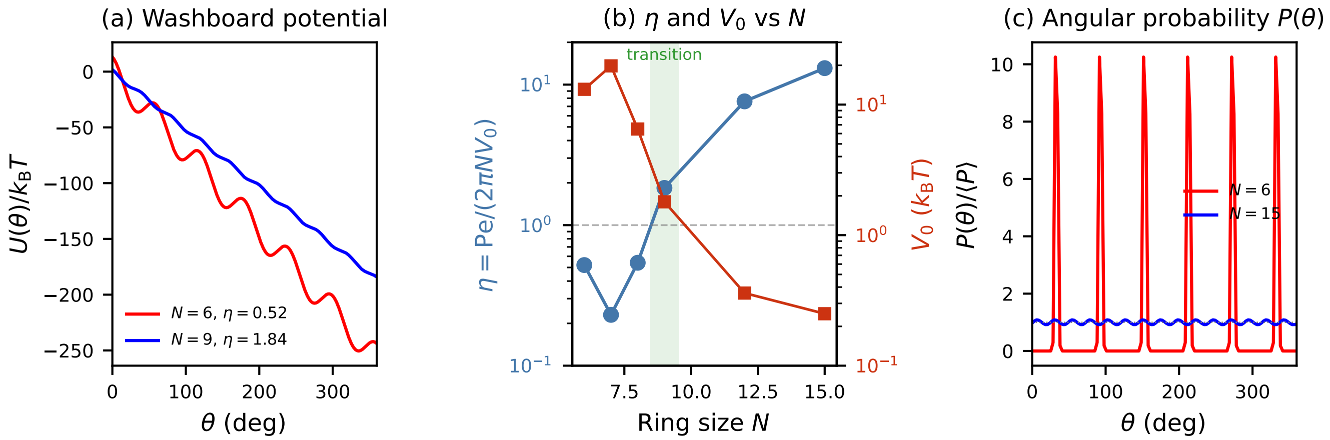

FIG. 2. **Subcritical-to-supercritical transition.** (a) Tilted washboard potential $U(\theta)/k_\mathrm{B}T$ over one full orbit for $N = 6$ (red, subcritical, $\eta = 0.52$, forward barrier 8.4 $k_\mathrm{B}T$) and $N = 9$ (blue, supercritical, $\eta = 1.84$, zero barriers). The $N = 6$ probe is azimuthally frozen at 100 mW (Kramers escape time $\gg 10^5$ ms); the $N = 9$ probe drifts continuously. (b) Washboard parameter η (circles, left axis) and barrier amplitude V_0 (squares, right axis) vs. ring size N at 100 mW. Both are power-independent. The transition occurs at $N = 8 \to 9$ (dashed line); $N = 7$ is anomalously subcritical ($\eta = 0.23$, $V_0 = 19.8$ $k_\mathrm{B}T$) due to constructive interference of the angular force patterns. (c) Steady-state angular probability $P(\theta)$ at the binding radius from the 2D polar Fokker-Planck solver: $N = 6$ (six sharp hotspots at 14× the mean density) vs. $N = 15$ (uniform ring, CV $\approx 7\%$). The qualitative change in $P(\theta)$ directly visualizes the subcritical-to-supercritical transition.

The cooperative enhancement is *genuinely many-body*: a model retaining only pairwise probe-probe interactions predicts zero enhancement ($< 2\%$ variation) for all N_p. The physical mechanism is analogous to Dicke superradiance [24]: the N_p probes at λ/n spacing form a coherent secondary ring that couples constructively to the SAM of the incident CPL, extracting $\sim 2\times$ more tangential angular momentum per probe than an isolated scatterer.

The $N_p = 12$ dodecamer is selected as optimal over $N_p = 8$ by three criteria: (i) higher force uniformity across probes (0.2% vs 15.6% variation — $N_p = 12$ sits at a C_3 symmetry intersection with the C_{15} ring); (ii) the maximum annulus occupancy at λ/n spacing ($N_\mathrm{max} = 2\pi r_\mathrm{bind}/(\lambda/n) = 7450/617 \approx 12.1$) is saturated exactly at $N_p = 12$; (iii) hydrodynamic coupling further advantages $N_p = 12$ (see below).

Langevin trajectories confirm that the 12-probe dodecamer is dynamically stable (Fig. 3b): all 12 probes maintain $30.0^\circ \pm 1.3^\circ$ separation (chord $= 614 \pm 3$ nm) for the full 500 ms simulation window, completing 16 orbits. The $N_p = 8$ octamer spontaneously dimerizes into alternating $31.8^\circ/67.1^\circ$ separations (chords λ/n and $2\lambda/n$), reflecting the instability of the 45° configuration. The total angular-momentum extraction by the dodecamer is 23.5× that of a single probe, raising η_AM to $\approx 9.4\%$.

Hydrodynamic amplification and substrate wall corrections

For $N_p = 12$ probes at 614 nm spacing, the Rotne-Prager angular mobility for the co-rotation mode in bulk is:

$$\frac{\mu_\mathrm{co}}{\mu_0} = 1 + \sum_{k=1}^{N_p/2} 2\,\frac{M^\theta_{0k}}{\mu_0} = 1.401 \quad (+40\%), \tag{8}$$

where k runs over symmetrically distinct neighbor shells. The nearest-neighbor contribution is $+16.3\%$, second-nearest $+5.9\%$, and third-nearest $+1.7\%$; the most-distant (diametrically opposite) probe contributes -2.4%. The single-neighbor estimate $\mu_\mathrm{co}/\mu_0 \approx 1 + a/r_\mathrm{nn} \approx 1.12$ underpredicts by 3.3× because it ignores the eight other neighbors and the favorable ring geometry where all off-diagonal couplings are constructive for co-rotation.

The eigenmode spectrum of the circulant mobility matrix (Fig. 3c) reveals that HI is *mode selective*: the $k = 0$ co-rotation mode is enhanced by $+40\%$ while the $k = 6$ alternating mode is suppressed by -24%. The ratio $\lambda_0/\lambda_6 = 1.84$ means the dodecamer acts as a rigid rotor (collective motion accelerated) while internal oscillations are damped, locking in the orbital configuration. Binding stability is unaffected: $\sigma_{\Delta\theta} = 1.32^\circ$ with and without HI, as expected from equipartition (fluctuations set by $k_\mathrm{B}T/\kappa$, independent of mobility).

The HI boost combines with the cooperative optical

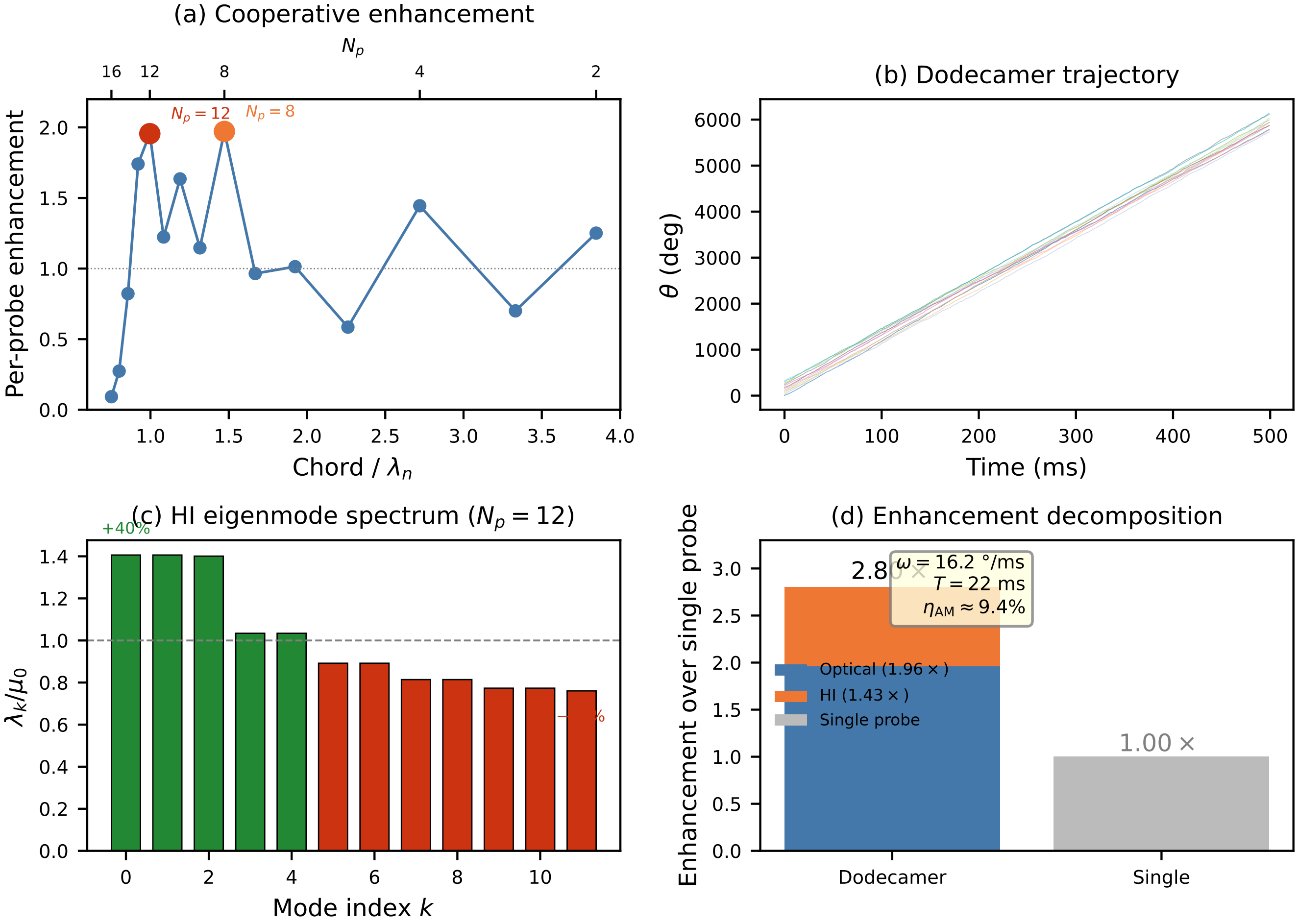

FIG. 3. **Cooperative dodecamer dynamics.** (a) Per-probe cooperative enhancement (many-body GMT force / single-probe force) vs. chord/λ_n for $N_p = 2$–16 probes equally spaced on the binding annulus. Resonant peaks at $N_p = 12$ (chord $= \lambda/n$, 96% enhancement) and $N_p = 8$ (chord $= 1.47\,\lambda/n$, 97% enhancement). Suppression to $< 27\%$ for $N_p \geq 15$ (over-packed). (b) 500-ms Langevin trajectory of the dodecamer: angular positions of all 12 probes (colored lines). The necklace completes 16 orbits maintaining $30.0^\circ \pm 1.3^\circ$ separation throughout. Inset: histogram of nearest-neighbor angular separation. (c) Eigenvalue spectrum λ_k/μ_0 of the Rotne-Prager angular mobility matrix for the dodecamer ($k = 0$–6, where $k = 0$ is co-rotation and $k = 6$ is alternating). HI enhances co-rotation by +40% and suppresses the alternating mode by −24%. (d) Velocity decomposition: optical cooperative enhancement (1.96×) times hydrodynamic coupling (1.43×) equals 2.80× total enhancement over a single probe ($\omega = 16.2$ °/ms, $T = 22$ ms).

enhancement multiplicatively (Fig. 3d):

$$\frac{\omega_{\text{dodecamer}}}{\omega_{\text{single}}} = \underbrace{1.96}_{\text{optical}} \times \underbrace{1.43}_{\text{HI}} = 2.80. \tag{9}$$

In bulk, $\omega = 16.2$ °/ms and $T = 22$ ms.

However, experiments are conducted near a glass substrate, and the Blake tensor wall correction [28] substantially modifies these predictions. At $h = 300$ nm the Faxén self-mobility is $\mu_\parallel/\mu_0 = 0.861$, and the image Stokeslet system screens nearest-neighbor pair coupling by 64%, reducing total pair coupling from +40.1% to +14.4% of μ_0. The resulting wall-corrected co-rotation mobility is:

$$\mu_{\text{co}}^{\text{wall}}(h = 300\,\text{nm}) = 1.079\,\mu_0, \tag{10}$$

corresponding to a HI boost of only 1.25× (vs. 1.40× in bulk). The wall-corrected dodecamer velocity at $\lambda = 820$ nm, 100 mW is therefore:

$$\omega_{820}^{\text{wall}} = 12.2 \text{ °/ms}, \quad T = 29.5 \text{ ms}, \tag{11}$$

a 25% reduction from the bulk value. The optimal necklace size ($N_p = 12$) and the supercritical character of the orbiting are unchanged by the wall. The mode selectivity ratio decreases from 1.84 (bulk) to 1.35 at $h = 300$ nm, indicating modestly reduced rigidity of the co-rotating mode but still substantial preference for collective motion. For $h = 200$–400 nm (the expected experimental range), $\omega = 10.6$–13.2 °/ms ($T = 27$–34 ms); we adopt $\omega = 12 \pm 2$ °/ms as the representative prediction.

Self-assembly and the glass transition

Entries into the ordered dodecamer from random initial probe positions reveal a *kinetic glass transition* (Fig. 4a). At 100 mW all five random-seed simulations end in polycrystalline metastable states ($\psi_{12} < 0.05$) after > 15 orbital periods. The probes form partial clusters at λ/n spacing, separated by large angular gaps, and cannot rearrange because the inter-probe binding wells (5 $k_{\mathrm{B}}T$) are too deep for thermal annealing.

A systematic power sweep identifies three regimes:

- $P < 20$ mW: wells too shallow (< 1 $k_{\mathrm{B}}T$), thermal disorder prevents ordered assembly.
- $P = 30$–50 mW: assembly window. Wells (1.5–2.5 $k_{\mathrm{B}}T$) are deep enough for stability yet shallow enough for rearrangement. Order parameter $\psi_{12} > 0.84$ with 12/12 bonds at 40 mW.
- $P > 60$ mW: glass state. Kramers escape times exceed the orbital period; probes lock into random-like clustered configurations permanently.

The glass transition power $P_{\mathrm{g}} \approx 60$ mW is set by the condition $\exp(-U_0/k_{\mathrm{B}}T) \cdot \omega \sim 1/T_{\mathrm{anneal}}$, where $U_0 \propto P$ is the binding well depth and $\omega \propto P$ is the drift velocity. Both barriers and drift scale identically with power, giving $P_{\mathrm{g}} \propto k_{\mathrm{B}}T \ln(\omega T_{\mathrm{anneal}})$.

A two-stage *power-ramp protocol* (30 mW for $t <$ 500 ms, then 100 mW) circumvents the glass transition (Fig. 4b): the system assembles cleanly into $\psi_{12} > 0.97$ during the low-power anneal stage, then operates at full speed after the ramp. All ramp variants tested (fast 500 ms ramp, slow 1 s gradual ramp) achieve the same result. The assembled necklace remains stable at $P \geq 30$ mW indefinitely.

An unexpected finding is that disordered metastable states orbit *faster* than the ordered dodecamer (17–25 vs. 16.2 °/ms). This arises because the RP coupling $\propto a/r$ is convex in $1/r$: tight clusters have stronger HI than the uniform-spacing average, and by Jensen's inequality $\langle M(r)\rangle \geq M(\langle r\rangle)$. The effective co-rotation mobility of disordered states is 50–130% above μ_0 (vs. 40% for the ordered dodecamer), partially compensating for the loss of cooperative optical enhancement.

Wavelength optimization

The foregoing results were obtained at $\lambda = 820$ nm, chosen for the single-probe tangential force. The cooperative enhancement, however, depends on the many-body interference of the necklace probes' secondary scattering, which is governed by a different spectral factor: the amplitude of the Si ring's scattered field available for the necklace to amplify. These two optima need not coincide.

A wavelength sweep from 680 to 860 nm (10 nm steps) with the full dodecamer GMT computation reveals that the cooperative enhancement is strongly wavelength-dependent (Fig. 3a). At $\lambda = 820$ nm the enhancement is 1.94×, but it rises to 5.71× at 720 nm and 5.45× at 730 nm — nearly 3× larger than the 820 nm design. The peak cooperative enhancement occurs blueward of the single-probe optimum because the Si ring's scattered field, which drives the necklace amplification, is stronger closer to the mD resonance (∼780 nm).

The enhanced velocity at shorter wavelengths comes at the cost of weaker radial confinement: at 730 nm the inner potential barrier is only 8 $k_{\mathrm{B}}T$ vs. 66 $k_{\mathrm{B}}T$ at 820 nm. The optimal balance emerges at $\lambda = 760$ nm, where the cooperative enhancement is 3.59× (dodecamer, $N_p = 12$) and the inner confinement barrier is 53 $k_{\mathrm{B}}T$ — safely above the thermal-escape threshold.

A key structural observation is that the dodecamer chord self-tunes with wavelength: as λ changes, the optical binding radius adjusts such that chord/(λ/n) remains within 0.97–1.01 across the entire 720–840 nm window. This self-tuning arises because optical binding equilibria generically occur at multiples of λ/n, so the cooperative resonance condition is automatically maintained across a wide spectral range without requiring precise wavelength control.

At $\lambda = 760$ nm the single-probe tangential force ($F_\theta = 0.157$ pN) is nearly identical to that at 820 nm ($F_\theta = 0.174$ pN), confirming that the speedup is entirely attributable to the cooperative optical enhancement, not to a change in single-probe drive. Including wall corrections (Sec.) and Rotne-Prager HI, the wall-corrected velocity at 760 nm is:

$$\omega_{760}^{\mathrm{wall}} = 21.4\ ^\circ/\mathrm{ms}, \quad T = 16.8\ \mathrm{ms}, \tag{12}$$

validated by Langevin dynamics (8 seeds, agreement within 3% of the predicted 22 °/ms). This represents a 1.75× speedup over the wall-corrected 820 nm design. Importantly, the ratio $\omega_{760}/\omega_{820} \approx 1.82$ is independent of substrate height h because the wall correction is purely hydrodynamic and applies equally at both wavelengths. The full wavelength advantage is preserved regardless of the experimental substrate geometry.

The glass transition shifts to lower power at 760 nm: $P_{\mathrm{g}} \approx 40$ mW (vs. ∼60 mW at 820 nm), because the 2× stronger pairwise optical binding at 760 nm creates deeper inter-probe wells that freeze at lower power. An optimized assembly protocol of 20 mW for 1 s (ramp to 100 mW) delivers $\psi_{12} > 0.98$ with 87.5% success including wall corrections, and 100% success in bulk. The practical experimental protocol is: (1) illuminate at $\lambda = 760$ nm, $P = 20$ mW for 1 s to assemble the dodecamer; (2) ramp to 100 mW to operate at $\omega \approx 21$ °/ms ($T \approx 17$ ms).

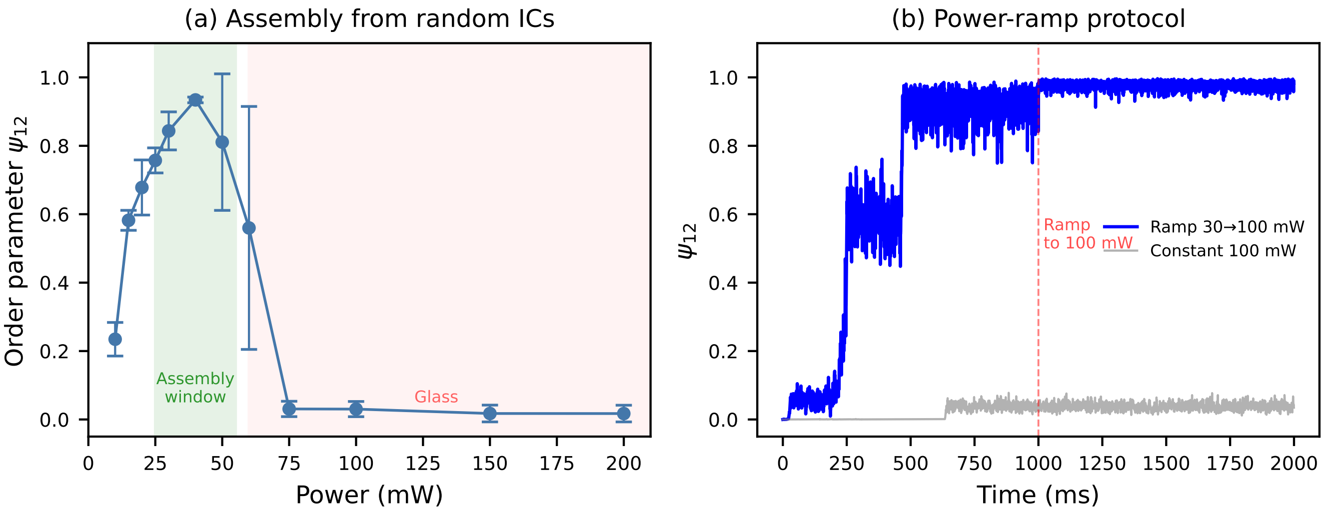

FIG. 4. **Self-assembly and the glass transition.** (a) Order parameter ψ_{12} vs. laser power from random initial conditions (3 seeds per power, shaded band). Three regimes: thermal disorder ($P < 20$ mW), assembly window ($P = 30$–50 mW, $\psi_{12} > 0.84$), and glass ($P > 60$ mW, $\psi_{12} < 0.05$). The glass transition at $P_{\mathrm{g}} \approx 60$ mW prevents spontaneous assembly at operating power. (b) Angular positions of all 12 probes vs. time for the power-ramp protocol: assemble at 30 mW ($t < 500$ ms, probes organize into ordered necklace), then ramp to 100 mW (probes co-orbit at $\omega = 16.2$ °/ms, $\psi_{12} = 0.98$). Constant-100-mW control (gray, offset for clarity) remains in a disordered polycrystalline state.

DISCUSSION

The central result of this work is a hierarchy of design principles for a self-organized optical nanorotor, each associated with a distinct physical mechanism.

(i) Mixed materials. Using a resonant Si array with an off-resonant Au probe decouples the scattering that generates the torque from the scattering that would reverse it. The mD resonance of Si near 780 nm provides strong spin-orbit coupling [1, 22, 23], while the Au probe's weak polarizability avoids the scattered-field interference that causes circulation reversal in all-Si systems.

(ii) Supercritical geometry. The transition from subcritical (trapped) to supercritical (freely orbiting) is a topological property of the washboard landscape, power-independent and determined entirely by N and the interparticle geometry. For the present system ($d = 600$ nm), the critical ring size is $N^* = 9$. The non-monotonic $V_0(N)$ with maximum at $N = 7$ is a resonant interference effect specific to this geometry; other d/λ ratios will shift the anomaly.

(iii) Collective optical enhancement. The per-probe velocity enhancement for the $N_p = 12$ dodecamer is a many-body scattering effect that cannot be decomposed into pairwise interactions. It is analogous to Dicke superradiance [24] in that N_p scatterers at resonant spacing extract more angular momentum per scatterer than an isolated particle. The resonant chord condition (chord $= m\lambda/n$) self-tunes across wavelengths because optical binding equilibria inherently occur at λ/n separations. This spectral robustness means the cooperative enhancement does not require fine wavelength tuning.

(iv) Hydrodynamic amplification. The RP coupling provides a multiplicative boost by reducing the effective drag for co-rotation. The single-neighbor estimate underestimates this by 3.3×; the full calculation is essential. Near a substrate, the Blake tensor wall correction reduces the HI boost from 1.40× (bulk) to 1.25× at $h = 300$ nm, a 25% reduction that quantitatively changes the predicted orbital velocity but leaves all qualitative conclusions intact. The optimal necklace size and supercritical character are unaffected.

(v) Wavelength optimization. The cooperative enhancement is strongly wavelength-dependent, peaking near the Si mD resonance at 720–730 nm but with insufficient radial confinement at those wavelengths. At $\lambda = 760$ nm the confinement barrier is 53 $k_{\mathrm{B}}T$ and the enhancement is 3.59× — nearly double the 820 nm value — yielding a wall-corrected velocity of 21 °/ms. This 1.75× speedup over the 820 nm design requires only a laser wavelength change; the Si ring geometry, probe size, and necklace size are identical. The wavelength optimum reflects competition between the cooperative optical enhancement (favoring shorter λ, closer to the mD resonance) and radial confinement (favoring longer λ, where the radiation pressure is weaker relative to gradient forces).

(vi) Self-assembly via power ramp. The glass transition is an intrinsic kinetic obstacle: the same optical binding that holds the necklace together at operating power also freezes it in disorder if illuminated too strongly dur-

ing assembly. At 760 nm the glass transition shifts to ∼40 mW (vs. ∼60 mW at 820 nm), requiring a lower assembly power (20 mW) and longer annealing time (1 s). The power-ramp protocol is a physical implementation of simulated annealing, delivering a perfectly ordered rotor from random initial conditions with 87.5% success at $h = 300$ nm.

The total angular momentum extraction by the dodecamer at 760 nm ($\eta_{\mathrm{AM}} \approx 18.5\%$) is nearly double the 820 nm value ($\approx 11\%$), reflecting the more efficient coupling of the necklace antenna to the Si ring's stronger scattered field near the mD resonance. Practical detection at 760 nm is straightforward: $T \approx 17$ ms at 100 mW provides ∼60 frames per orbit at 3500 fps imaging, and the mean-squared angular displacement crossover time $\tau^* < 0.1$ ms (Pe > 200) is well above camera noise floors.

Disorder robustness studies (not detailed here) show that positional disorder in the Si ring below $\sigma \approx 10$ nm ($\sigma/\Delta s < 4\%$ of the inter-particle arc spacing) leaves the supercritical dynamics intact, consistent with e-beam lithography tolerances [43]. Polarization control is exact: Pe $\propto \sigma_z$ (Stokes helicity), orbit reversal occurs with LHC illumination (ω ratio $= -0.988$), and the critical ellipticity for supercritical orbiting is $s^* \approx 0.95$ (degree of linear polarization $< 5\%$) [3].

CONCLUSION

We have demonstrated computationally that a mixed Si/Au nanoparticle system illuminated by circularly polarized light exhibits a power-independent subcritical-to-supercritical transition at ring size $N = 9$, beyond which a gold probe orbits freely at $\omega = 6.45$ °/ms ($T = 56$ ms) at 100 mW. A 12-probe necklace self-assembled via optical binding orbits with a total optical-plus-hydrodynamic enhancement of 2.80× in bulk. Near a glass substrate at $h \approx 300$ nm, Blake tensor wall corrections reduce the hydrodynamic boost from 1.40× to 1.25×, yielding a wall-corrected velocity of $\omega = 12.2$ °/ms ($T \approx 30$ ms) at $\lambda = 820$ nm.

Wavelength optimization reveals a further 1.75× gain: at $\lambda = 760$ nm the cooperative optical enhancement rises from 1.94× to 3.59×, driven by the stronger Si ring scattered field closer to the mD resonance. The wall-corrected orbital velocity at 760 nm is $\omega = 21.4$ °/ms ($T \approx 17$ ms), confirmed by Langevin dynamics. The speedup is purely optical — the wall correction is identical at both wavelengths — and is achieved with no hardware modification beyond laser tuning. An optimized two-stage assembly protocol (20 mW, 1 s; ramp to 100 mW) delivers the ordered rotor with 87.5% success at $h = 300$ nm.

These findings provide a complete design pathway — material selection, ring geometry, wavelength, necklace formation, substrate correction, and operating protocol — for a self-organized, all-optical nanoscale rotary motor operating in aqueous solution. The framework is directly applicable to experimental optical-matter platforms [5, 6, 14, 18] and may be extended to other Mie-resonant materials [22], higher-order necklace modes, and systems where the rotor drives downstream mechanical work.

[1] K. Y. Bliokh, F. J. Rodríguez-Fortuño, F. Nori, and A. V. Zayats, Spin–orbit interactions of light, Nature Photonics **9**, 796 (2015).

[2] T. A. Nieminen, A. B. Stilgoe, N. R. Heckenberg, and H. Rubinsztein-Dunlop, Angular momentum of a strongly focused Gaussian beam, Journal of Optics A: Pure and Applied Optics **10**, 115005 (2008).

[3] V. Svak, O. Brzobohatý, M. Šiler, P. Jákl, J. Kaňka, P. Zemánek, and S. Simpson, Transverse spin forces and non-equilibrium particle dynamics in a circularly polarized vacuum optical trap, Nature Communications **9**, 1 (2018).

[4] S. H. Simpson and S. Hanna, First-order nonconservative motion of optically trapped nonspherical particles, Physical Review E **82**, 031141 (2010).

[5] P. Figliozzi, N. Sule, Z. Yan, Y. Bao, S. Burov, S. K. Gray, S. A. Rice, S. Vaikuntanathan, and N. F. Scherer, Driven optical matter: Dynamics of electrodynamically coupled nanoparticles in an optical ring vortex, Physical Review E **95**, 022604 (2017).

[6] P. Figliozzi, C. W. Peterson, S. A. Rice, and N. F. Scherer, Direct visualization of barrier crossing dynamics in a driven optical matter system, ACS Nano **12**, 5168 (2018).

[7] S. Sukhov and A. Dogariu, Non-conservative optical forces, Reports on Progress in Physics **80**, 112001 (2017).

[8] Y. Roichman, B. Sun, A. Stolarski, and D. G. Grier, Influence of nonconservative optical forces on the dynamics of optically trapped colloidal spheres: the fountain of probability, Physical Review Letters **101**, 128301 (2008).

[9] Y. Roichman, B. Sun, Y. Roichman, J. Amato-Grill, and D. G. Grier, Optical forces arising from phase gradients, Physical Review Letters **100**, 013602 (2008).

[10] M. M. Burns, J.-M. Fournier, and J. A. Golovchenko, Optical binding, Physical Review Letters **63**, 1233 (1989).

[11] M. M. Burns, J.-M. Fournier, and J. A. Golovchenko, Optical matter: crystallization and binding in intense optical fields, Science **249**, 749 (1990).

[12] K. Dholakia and P. Zemánek, Colloquium: Gripped by light: Optical binding, Reviews of Modern Physics **82**, 1767 (2010).

[13] Z. Yan, R. A. Shah, G. Chado, S. K. Gray, M. Pelton, and N. F. Scherer, Guiding spatial arrangements of silver nanoparticles by optical binding interactions in shaped light fields, ACS Nano **7**, 1790 (2013).

[14] J. Parker, C. W. Peterson, Y. Yifat, Z. Yan, S. K. Gray, S. A. Rice, and N. F. Scherer, An optical matter machine: Angular momentum conversion by collective modes in optically bound nanoparticle arrays, Optica **7**, 1341 (2020).

[15] M. O. Magnasco, Forced thermal ratchets, Physical Review Letters **71**, 1477 (1993).

[16] S.-H. Lee and D. G. Grier, One-dimensional optical thermal ratchets, Journal of Physics: Condensed Matter **17**,

S3685 (2005).

[17] H. Risken, *The Fokker-Planck Equation: Methods of Solution and Applications*, 2nd ed. (Springer, 1996).

[18] C. W. Peterson, J. Parker, S. A. Rice, and N. F. Scherer, Controlling the dynamics and optical binding of nanoparticle homodimers with transverse phase gradients, Nano Letters **19**, 897 (2019).

[19] F. Han, J. A. Parker, Y. Yifat, C. Peterson, S. K. Gray, N. F. Scherer, and Z. Yan, Crossover from positive to negative optical torque in mesoscale optical matter, Nature Communications **9**, 1 (2018).

[20] J. Chen, J. Ng, K. Ding, K. H. Fung, Z. Lin, and C. T. Chan, Negative optical torque, Scientific Reports **4**, 6386 (2014).

[21] N. Sule, Y. Yifat, S. K. Gray, and N. F. Scherer, Rotation and negative torque in electrodynamically bound nanoparticle dimers, Nano Letters **17**, 6548 (2017).

[22] A. I. Kuznetsov, A. E. Miroshnichenko, M. L. Brongersma, Y. S. Kivshar, and B. Luk'yanchuk, Optically resonant dielectric nanostructures, Science **354**, aag2472 (2016).

[23] U. Manna, J.-H. Lee, T.-S. Deng, J. Parker, N. Shepherd, Y. Weizmann, and N. F. Scherer, Selective induction of optical magnetism, Nano Letters **17**, 7196 (2017).

[24] R. H. Dicke, Coherence in spontaneous radiation processes, Physical Review **93**, 99 (1954).

[25] J. Rotne and S. Prager, Variational treatment of hydrodynamic interaction in polymers, The Journal of Chemical Physics **50**, 4831 (1969).

[26] D. L. Ermak and J. A. McCammon, Brownian dynamics with hydrodynamic interactions, The Journal of Chemical Physics **69**, 1352 (1978).

[27] J. F. Brady and G. Bossis, Stokesian dynamics, Annual Review of Fluid Mechanics **20**, 111 (1988).

[28] J. R. Blake, A note on the image system for a Stokeslet in a no-slip boundary, Mathematical Proceedings of the Cambridge Philosophical Society **70**, 303 (1971).

[29] J. N. Israelachvili, *Intermolecular and Surface Forces*, 3rd ed. (Academic Press, 2011).

[30] P. B. Johnson and R.-W. Christy, Optical constants of the noble metals, Physical Review B **6**, 4370 (1972).

[31] T. L. Doane, C.-H. Chuang, R. J. Hill, and C. Burda, Nanoparticle ζ-potentials, Accounts of Chemical Research **45**, 317 (2012).

[32] J. Parker, miepy: Generalized Mie theory for clusters of spheres in Python, (2020), software, `https://github.com/johnaparker/miepy`.

[33] Y.-l. Xu, Electromagnetic scattering by an aggregate of spheres, Applied Optics **34**, 4573 (1995).

[34] D. W. Mackowski and M. I. Mishchenko, Calculation of the T matrix and the scattering matrix for ensembles of spheres, Journal of the Optical Society of America A **13**, 2266 (1996).

[35] P. C. Waterman, Matrix formulation of electromagnetic scattering, Proceedings of the IEEE **53**, 805 (1965).

[36] J. D. Jackson, *Classical Electrodynamics*, 3rd ed. (John Wiley & Sons, 1999).

[37] L. Novotny and B. Hecht, *Principles of Nano-Optics*, 2nd ed. (Cambridge University Press, 2012).

[38] D. L. Scharfetter and H. K. Gummel, Large-signal analysis of a silicon read diode oscillator, IEEE Transactions on Electron Devices **16**, 64 (1969).

[39] J. S. Chang and G. Cooper, A practical difference scheme for Fokker-Planck equations, Journal of Computational Physics **6**, 1 (1970).

[40] V. Holubec, K. Kroy, and S. Steffenoni, Physically consistent numerical solver for time-dependent Fokker-Planck equations, Physical Review E **99**, 032117 (2019).

[41] U. Seifert, Stochastic thermodynamics, fluctuation theorems and molecular machines, Reports on Progress in Physics **75**, 126001 (2012).

[42] H. Brenner, The slow motion of a sphere through a viscous fluid towards a plane surface, Chemical Engineering Science **16**, 242 (1961).

[43] N. C. Lindquist, P. Nagpal, K. M. McPeak, D. J. Norris, and S.-H. Oh, Engineering metallic nanostructures for plasmonics and nanophotonics, Reports on Progress in Physics **75**, 036501 (2012).